Development of the UV and Visible Impurity Influx Monitor (Divertor) for ITER

Atsushi Iwamae, Hiroaki Ogawa, Tatsuo Sugie, Satoshi Kasai, Yoshinori Kusama

Japan Atomic Energy Agency, Mukoyama 801-1, Naka, Ibaraki,311-0193, Japan

Nippon Advanced Technology, Tokai, Ibaraki, 311-1112, Japan

We have developed a spectroscopic diagnostics system in the wavelength region of 200 - 1000 nm for monitoring ITER divertor plasmas, such as the influx of impurity elements, position of the ionization front, electron temperature and density. An equivalent size prototype of the optical components for the upper port spectroscopic diagnostics system has been fabricated and assembled as part of the system to estimate quantitative light throughput. Collisional-radiative models estimate the line intensities of helium ash and carbon ions. The reflection of tungsten and carbon fiber composite, which comprise the plasma facing materials of the divertor, is measured. The reflection of the surface of the tungsten divertor material is 23% at λ656nm. There is an anisotropic aspect to the surfaces of W and CFC.

Keywords: iter divertor plasma, spectroscopic diagnostics, impurity influx, in-site calibration method, reflection of divertor component materials

1. Introduction

Generating electric power by means of nuclear fusion, DEMOs, and the next generation of tokamak- and heliotron-type reactors of ITER, has been proposed, including the SlimCS [1]. In order to realize the potential of a DEMO reactor, the plasma diagnostics in the harsh environment of D-T fusion plasmas, i.e., high levels of neutrons, gamma-rays and plasma particle bombardment as well as nuclear heating, should be strictly tested during the ITER phase. The impurity influx monitor (divertor) through ultra-violet (UV) and visible spectroscopic measurements [2-4] is responsible primarily for monitoring influx from the plasma-facing components of beryllium, carbon, and tungsten, for sensing the position of the ionization front, and for determining the ion temperature in divertor plasmas [5]. The impurity influx monitor also has the secondary functions of monitoring electron temperature and density (T_e and n_e), as well as the fuel ratios (n_H/n_D or n_T/n_D) of divertor plasmas. The impurity influx monitor also supplements information about the radiation power and profiles in the divertor and the X-point/MARFE regions, and gives information about the densities of neutral atoms and molecules.

The neutron flux and energy deposition in mirror materials and the vacuum window are estimated in Ref. [6]. Estimates of the neutron flux and nuclear heating at the first mirror located ~1m behind the first wall are 1.2×10^8 m^{-2} s^{-1} and 20 kW/m^3, respectively. It is known that neutron irradiation of 1.4×10^8 n m^{-2} on the molybdenum mirror has no effect on the mirror surface [7]. Divertor

systems are planned for the upper #01, equatorial #01 and divertor #02 ports. The fist mirrors of these systems are made of molybdenum. From each of the upper and equatorial ports, we may observe the divertor plasma with lines of sight in a 71 chord fan array. From the divertor port we observe the plasma with viewing chords in a fan array placed in a gap between the divertor cassettes. The optical design of the viewing chords for observing strike divertor plate is undergoing to fit inside the new divertor dome box. Here we report on the present status of development of the divertor for ITER on the upper port.

2. Prototype optical properties

We have assembled the optical components into a scale size model viewing system. Figure 1 shows the arrangement of the upper port optical system. The prototype of the upper port fan array viewing chords is manufactured with fifty lines of sight, though seventy-one lines are planned for the production model. The front-end optics placed close to the main plasma consists of three metallic mirrors. The material of the first and second mirrors is molybdenum. The second is an off-axis paraboloid mirror. The third is a plane aluminum. The distance from the first mirror to the divertor dome is about eight meters. The fifty lines of sight cover 1.4 m in the poloidal direction. Emissions from the divertor plasma collected with the front-end optical optics are transferred via a dog-leg, using two aluminum-coated glass mirrors with a 190 mm effective diameter to a Cassegrain telescope.
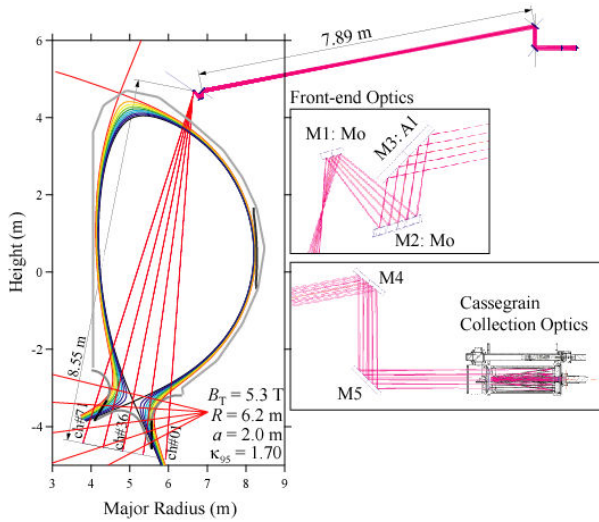
Fig.1 The upper port optical system of the impurity influx monitor (divertor). Front-end optics consists of three metallic mirrors: a plane M1(Mo), an off-axis paraboloid M2(Mo), and a plane M3(Al). Fan array lines of observation are planned to total seventy-one chords from the upper port.

At the focus plane of the Cassegrain collection optics, a micro-lens array is coupled with fifty optical fibers whose 200-micrometer core diameter is contained within a 220-micrometer clad. The micro lens array (MLA) is made of synthetic silica and contains in one unit, ten biconvex lens with a radius, length, and height of 3.3 mm, 6.7 mm, and 2mm, respectively. These five units are bonded with a binding material. Fifty optical fibers of two meters each transfer the light to a spectrometer, each of which has an FC coupler.

We measured the light throughput coefficient of the prototype. A calibrated standard xenon light source irradiated a Spectralon reflectance target at a distance of 50 cm. The target was placed 30 cm in front of the first mirror. A compact optical fiber-coupled spectrometer was used to record the spectral properties. Light to the spectrometer was relayed via a 20-meter length of the 200-220 FC-SMA optical fiber which prevents an anisotropic mode inside the core of the optical fiber.

Figure 2 shows the spectral throughput coefficients of three chords of #01, #26 and #50. In the visible wavelength region, the coefficient is almost flat at 4×10^{-11} m^2sr, and gradually decreases in the red wavelength region. Below a wavelength of 300 nm, the signal to noise ratio is rather low because of the spectrometer grating and detector efficiency. Above 800 nm no calibration data are available for the light source. Future experiments in the longer wavelength region will employ a calibrated integral
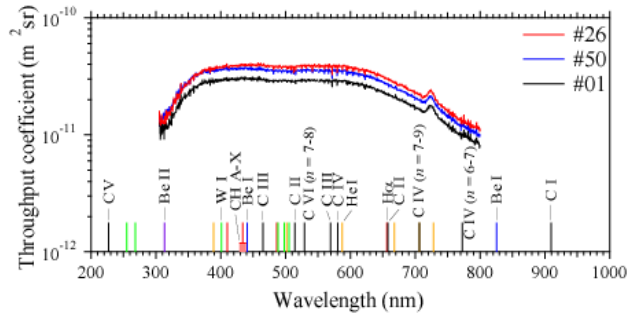

Fig.2 Measured light throughput coefficients for the upper port prototype. The peaks at the 730 nm are the pseudo-peak of the xenon line from the light source.

sphere.

The observable region of the MLA was assessed by means of inserting light from a halogen lamp into each of the optical fibers. The image when focused at the target plate at a distance of 8.55 m from the first mirror and gathered through the collection and front-end optical components,

Figure 3 shows an example of the MLA images. The widths of the examined lens image at 90% intensity range from 27 to 34 mm. This satisfies the ITER requirement of a 50 mm resolution. The surface of lens #01 is rather rough, such that the light throughput of this chord is relatively low. Where a micro lens array with a biconvex radius of $r = 2.45$ mm and length of 7.45 mm is feasible, light collection efficiency increases at least three times.
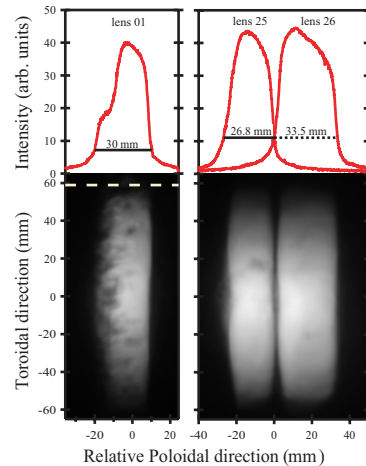

Fig.3 MLA image in the divertor region. The size of the image in the poloidal direction satisfies the ITER requirement of 50 mm.

3. Emission intensity estimation

Emission intensity of the ITER divertor plasma using the B2-EIRENE code package [8] has been calculated with the following conditions: $I_p = 15$ MA, $B_T = 5.3$ T, $P_{fusion} = 600$ MW, ($Q = 20$, $P_{NBI} = 30$ MW), a

deuterium flux from the core of 9×10^{21} s^{-1}, and a gas-puff rate of 1.4×10^{23} s^{-1}[9]. A two-dimensional plasma parameter distribution (T_e and n_e) and helium atom and ion density distributions are obtained from the code. Near the strike points in front of the inner and outer divertor targets, the plasma temperature is $T_e < 1$ eV and the density is $n_e > 1\times10^{21}$ m^{-3} I, leading to the conclusion that a detached plasma is formed. The line integrated emission intensity of He I lines is estimated with a collisional-radiative (CR) model [10,11]. Figure 3 shows one example (He I 2^3P – 3^3D, $\lambda587.6$ nm emission line radiance) of six emission lines of He I ($n = 3 - 2$), for both (a) ionizing and (b) recombining components. The chord-integrated intensity along the line-of-sight portrayed in Fig. 1 from the upper port is shown in Fig. 5. The peak intensity is 7×10^{17} ph s^{-1}m^{-2}sr^{-1}. The ionizing component is dominant for all of the observation chords since both strike points at the divertor plates are not observable from the upper port. The intensity ratios of the $I_{667.8 \text{ nm}}/I_{728.1 \text{ nm}}$ and $I_{728.1 \text{ nm}}/I_{706.5nm}$ emission lines are often used to estimate n_e and T_e. The singlet and triplet emission line-integrated intensities are plotted on a logarithmic scale as shown in Fig. 6. In order to obtain the n_e and T_e distributions, it is required to measure the radiance on the order of 10^{15} ph s^{-1}m^{-2}sr^{-1}.

component is dominant for all viewing chords.

The optical throughput coefficient is around 4×10^{-11} m^{2}sr, and peak photon intensity is 7×10^{17} ph s^{-1}m^{-2}sr^{-1}. If we divide the signal among three spectrometers, (UV, filter and High resolution), the efficiency of the split optical fibers is 12%. The light is transferred from the ITER port to the diagnostic room via one hundred meters of optical fiber with a transmission rate of 70%. If we use a spectrometer with a diffraction efficiency of ~50% and a back-illuminated CCD whose quantum efficiency is 60%, then 7.1×10^5 photoelectrons s^{-1} are detectable, i.e. 710 photoelectrons/ms. Helium ash that has a higher signal is observable with a 1 ms time resolution. However, to obtain special information on n_e and T_e, a certain amount of time is required. B2-EIRENE code also provides a C^{3+} and C^{4+} ion density map. We have estimated the C IV emission intensity using the CR model [12]. Results are shown in Fig. 7. The C IV (n= 6–7) 772.6 nm line is used to estimate ion temperature [13]. The upper port observes the divertor plasma through the high-temperature core plasma. Figure 8 shows the estimated bremsstrahlung continuum emission intensity along the central chord of the fan array view. The continuum emission is the same order for helium and the C IV emission intensity evaluated here.
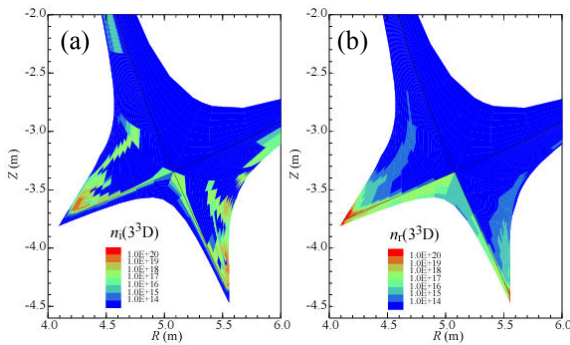

Fig.4 The population distribution of the n(3^3D) state, with (a) the ionizing component from helium atoms and (b) the recombining component from helium ion shown separately.
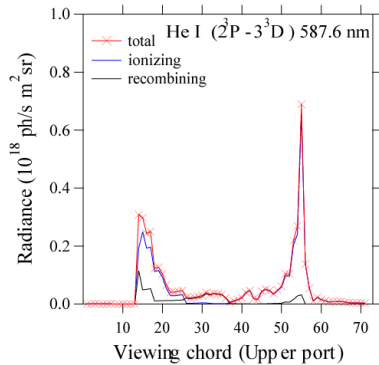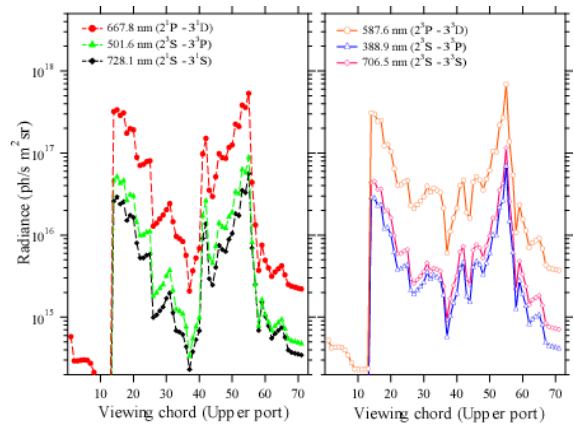

Fig.6 Chord-integrated emission intensity of the He I n = 3 to n = 2 levels.

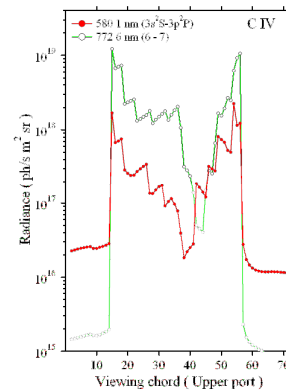Fig.5 Chord-integrated emission intensity of the He I 587.6 nm (2^3P – 3^3D) transition. The ionizing

Fig.7 Chord-integrated emission intensity of C IV.

Signal level shifts in the continuum radiation also are taken into account in evaluating the impurity emission intensities.
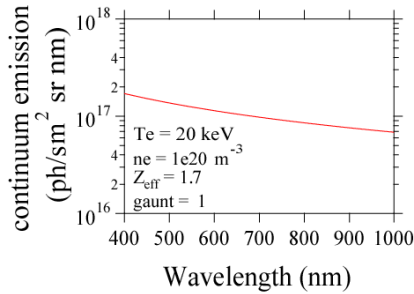

Fig.8   Bremsstrahlung intensity is the same order across impurity emission lines.

4. Spatial resolution with computer tomography

The position of the ionization front can be measured through a multi-chord observation. Spatial distribution with a full width of 10-cm at a half-maximum (FWHM) Gaussian distribution is examined as a model case.   In the #01 section we have an upper and equatorial fan array view, though the angle between the two views is rather narrow.   Neither strike points are covered by both upper and equatorial views.   We have employed the maximum entropy method [12,13] of the computerized tomopgraphy in order to reconstruct the two-dimensional special distribution.   The distribution of the reconstructed model is elongated along the vertical direction by a factor of four, compared to the original distribution.   In order to improve this situation we have proposed a gap-viewing fan array of 72 chords at divertor port #02 in the left gap of the central cassettes, looking radially inward.   We have to assume that the following reconstruction is based on toroidal symmetry at ports #02 and #01 of about 20 degrees in the toroidal direction. Figure 9 shows the suggested gap-viewing chords and the reconstructed image.   The reconstructed image with the upper port view and the gap fan array view provides a good estimate of the original distributions.
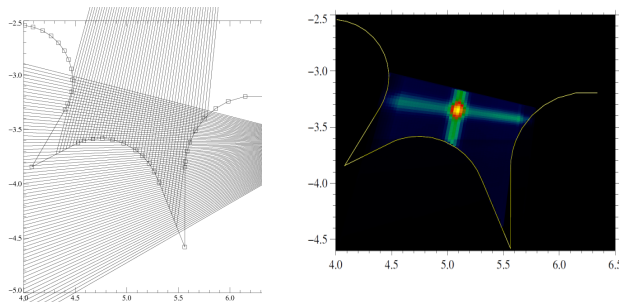

Fig.9   The gap-viewing chords and the CT image.

5. Reflection of the plasma-facing components.

The upper baffles of the inner and outer divertor and the dome are made of pure tungsten.   The strike points are carbon fiber composite (CFC).   We have examined the direct reflections of both divertor materials with injection light beams up to five degrees away from normal.   Spectral reflection measurements have been carried out with a spectrophotometer (JASCO V570 with a SLM468 unit).   Figure 10 shows the results for the CFC and tungsten divertor components.   CFC reflection is negligible, with a reflection peak of 0.5% at λ250 nm. However, the reflection of tungsten is as high as 23% at λ656 nm (Dα line).   There is an anisotropic aspect to the reflection because of the curved cutting by the milling machine.   We will investigate the bidirectional reflection distribution functions of the divertor material for lines at various wavelengths.
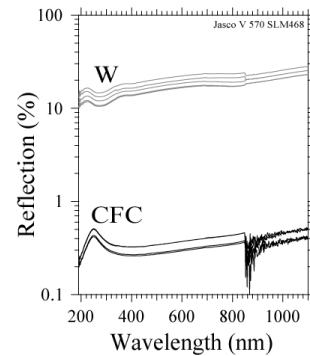

Fig.10   The five degree nominal reflections for W and CFC.   At a wavelength of 850 nm, the grating of the monochromator is changed, and the detectors are switched from a photomultiplier to a PbS sensor.

References

[1]   K. Tobita *et al.*, Nucl. Fusion **47**, 892 (2007).
[2]   T. Sugie *et al. Burning Plasma Diagnostics* (AIP, New York 2008) p. 218.
[3]   T. Sugie, J. Plasma Fusion Res **79**, 10 (2003).
[4]   H. Ogawa *et al.* Plasma and Fusion Res. **2**, S1054 (2007).
[5]   A. Costley, *System Require Document (SRD) Diagnostics* PBS 55 (2008).
[6]   H. Iida *et al. Nuclear Analysis Report* G 73 DDD 2 W 0.2 (2004).
[7]   T. Nishitani *et al*. Fusion Eng. Des. **42**, 443 (1998).
[8]   R. Schneider *et al*. J. Nucl. Mater. **266-269** 175 (1999).
[9]   A.S. Kukushkin *private communication*.
[10]   M. Goto, J. Quant. Spectro. Radiat. Trans. **76** 331 (2003).
[11]   M. Goto and T. Fujimoto, NIFS-DATA-043 (1997).
[12]   T. Nakano *et al*. Nucl. Fusion **47** 1458 (2007)..
[13]   T. Nakano *et al.* J. Plasma Fusion Res. **80**, 500 (2004).
[14]   N. Iwama and S. Ohdachi, J. Plasma Fusion Res. **82**, 399 (2006).
[15]   K. Fujimoto *et al.* Plasma Fusion Res. **2** S1121 (2007).